H. Kaneko[1], S. Ito[2], and K. Sasaki[1]

[1]Mutsu Institute for Oceanography, Research Institute for Global Change, Japan Agency for Marine-Earth Science and Technology, Kitasekine 690, Sekine, Mutsu, Aomori, 035-0022, Japan

[2]Atmosphere and Ocean Research Institute, The University of Tokyo, Kashiwanoha 5-1-5, Kashiwa, Chiba 277-8564, Japan

Corresponding author: Hitoshi Kaneko (h_kaneko@jamstec.go.jp)

Key Points:

- The distribution of chlorophyll a in global mid-latitude basins was studied in relation to eddy activity.
- The characteristic scale of the chlorophyll a distribution is closer to the deformation radius in regions of high meso-scale eddy activity.
- Larger horizontal scales of ~1000 km were found in eastern and central regions of each basin, with higher sensitivity to eddy activity.

Abstract

Understanding of the spatial distribution of near-surface oceanic chlorophyll a (Chl-a) in relation to eddy activity is important because Chl-a is critical to biological production and carbon absorption, and its distribution is closely related to meso-scale eddies and Rossby waves. Chl-a distributions based on satellite observations from 2001 to 2018 were analyzed in association with eddy activity in mid-latitude regions of the five ocean basins (North/South Pacific, North/South Atlantic, and South Indian oceans) and related to physical eddy scales including the internal Rossby deformation radius (L_{D}) and Rhines scale (L_{R}). In the open ocean, the horizontal scale of Chl-a (D) decreased with increasing eddy kinetic energy (EKE), converging to L_{D} in the high-eddy-activity region. The ratio of zonal (D_{z}) to meridional (D_{m}) scales, R_{D} ($= D_{\mathrm{z}}/D_{\mathrm{m}}$), converged to 1 with increasing EKE, implying isotropic uniformization with meso-scale eddies. In regions of low EKE (especially the central subtropical and eastern parts of each basin), D_{m} was larger than L_{D}, with a scale similar to L_{R}. In these regions, D_{z} values greater than D_{m} were found (with scales of 500–1000 km), indicating the effects of planetary phenomena on Chl-a. In such regions the sensitivity of D to EKE tended to be higher than in western boundary regions, indicating the influence of meso-scale eddy activity on the Chl-a distribution, even with low EKE.

Plain Language Summary

Chlorophyll a (Chl-a) is a pigment critical for photosynthesis and provides a representative index of phytoplankton activity that sustains oceanic ecosystems. To investigate the relationship between Chl-a distribution and eddy activity at various scales in global oceans, long-term satellite data were evaluated to obtain representative scales of Chl-a distribution (D) for comparison with oceanic

spatial scales, particularly with the internal Rossby deformation radius (L_{D}, up to 100 km) and the Rhines scale (L_{R}, hundreds to a million km). D is generally smaller than or similar to L_{D} in the western boundary of each ocean basin where meso-scale eddies are active, whereas it tends to be larger in the eastern and central subtropical basin areas with less meso-scale eddy activity. In these regions, eddy enlargement in the meridional direction is restricted by the effect of planetary rotation, and Chl-a information is stretched in the zonal direction like as the bands of Jupiter. However, the sensitivity of the horizontal scale of Chl-a to eddy activity tended to be higher than in the western boundary region, suggesting that a slight increase in meso-scale activity can influence Chl-a distribution in eastern parts of the basins.

1 Introduction

Ocean eddies are widespread (e.g., Nilsson and Cresswell, 1980; Joyce et al., 1984; Byrne et al., 1995; Gründlingh 1995; Qiu, 1995, 1999; Ridgway and Dunn, 2003; Itoh and Yasuda, 2010) and crucially important for the distribution of heat and nutrients in global oceans (e.g., Chelton et al., 2011a; McGillicuddy, 2016). Eddies also affect the distribution of Chlorophyll a (Chl-a), which is critical to biological production and carbon absorption in the global ocean. The relationship between eddies and Chl-a distribution has been investigated previously for non-linear meso-scale eddies ($O(100)$ km scale; e.g., Garcia et al., 2004; Chelton et al., 2011a; Lehahn, 2011; McGillcudy, 2016; Gaube and McGillicuddy, 2017) and Rossby waves (~1000 km scale; Cipollini et al., 2001; Uz et al., 2001; Seagel, 2001; Killworth et al., 2004).

Meso-scale eddies affect the Chl-a distribution by eddy pumping associated with isopycnal heaving caused by cyclonic eddies (e.g., McGilicuddy et al., 1998), with horizontal advection of ambient Chl-a along the periphery (Abraham, 1998; Siegel et al., 2007, 2011; Chelton et al., 2011a). Local Ekman pumping through interaction with surface wind (with convergence in cyclonic eddies and divergence in anticyclonic eddies; Siegel et al., 2011), sub-meso-scale upwelling around a meso-scale eddy (Levy et al., 2001), and vertical fluxes of nutrients occur during eddy development and decay and also affect Chl-a distributions (Folkowski et al., 1991). The influence of eddies on stratification also plays an important role in the distribution of Chl-a through suspension of phytoplankton under preferable light conditions (Levy et al., 1998; Gaube et al., 2013). Westward-propagating oceanic Rossby waves of planetary scale ($O(1000)$ km) may also affect Chl-a distributions through horizontal advection of a mean background Chl-a gradient, with vertical upwelling of nutrients and Chl-a (e.g., Killworth et al., 2004).

The importance of nonlinearity in meso-scale eddies has been considered in recent studies (e.g., Chelton et al., 2007; 2011a) with the development of satellite observations, providing a Lagrangian perspective on eddy formation and propagation. For example, Gaube et al. (2014) investigated the influence of mesoscale eddies on Chl-a distribution, focusing on variations of individual eddy interiors within an eddy-centric framework. Such an approach allows the study of trapped

fluid and properties of the eddy. However, a wider geophysical approach (a Eulerian perspective) is also important in elucidating the effects of eddy activity (including at scales larger than meso-scale eddies) on biogeographical functions, particularly concerning when we consider the regional dependence of eddy activity. Most energetic eddies occur in western ocean-boundary regions (Olson, 1991; Ducet et al., 2000; Chelton et al., 2011b). In contrast, Rossby waves are frequently generated in the eastern part of each basin and subsequently propagate to the western part (e.g., Gill, 1982). In regions where meso-scale eddies are weak but Rossby wave excitation is active, care should be taken in selecting the spatial scale of interest when considering Chl-a variation and related phenomena.

Here we attempt to elucidate the global distribution of surface Chl-a, its relationship to eddy activity, and specific features of the relationship in five basins—the North/South Pacific (NP/SP), North/South Atlantic (NA/SA), and South Indian (SI) oceans—using long-term data for Chl-a surface velocity fields provided by satellites. In particular, we investigate Chl-a distributions at scales representative of the oceans, namely the internal Rossby deformation radius and Rhines scales (Rhines, 1975; 1977) in relation to the magnitude of eddy kinetic energy (EKE), as differences from long-term temporal averages. The former suggests an effect of meso-scale eddies and the latter implies the planetary -effect (i.e., the effect related to meridional variation in the Coriolis parameter) on Chl-a distributions through two-dimensional turbulence. We also examine the isotropy/anisotropy of Chl-a distributions in two orthogonal directions (zonal and meridional) in relation to the role of eddies, including horizontal advection at the periphery of eddies and localities of sensitivity of Chl-a variations to eddy activity. Although satellite data products employed in this study do not resolve sub-meso-scale phenomena (Levy et al., 2012; Gaube et al., 2014), the indicated relationships improve our understanding of their features.

The paper is organized as follows. In section 2, data provided by satellites and processing methods are described and proposed indices are depicted. In section 3, relationships between Chl-a distributions and EKE are considered, comparing their scales with the internal Rossby deformation radius. Ratios of zonal to meridional scales of Chl-a distribution are discussed, considering the effects of intense temporal-mean flows, such as the Gulf Stream and the Kuroshio Extension. We also focus on the latitudinal distribution of zonal and meridional scales, comparing them with the Rhines scale to demonstrate the effect of two-dimensional turbulence on Chl-a distribution, with Chl-a variations converging to the internal Rossby deformation radius in the western part of each basin while being closer to the Rhines scale in the eastern and central parts. Finally, in section 4, we discuss the local effects of the sensitivity of Chl-a distributions within each basin. Higher sensitivity of Chl-a distribution to eddy activity in eastern parts of the basins is indicated, although mean EKE in these regions are smaller than in western parts of the basins.

2 Materials and Methods

2.1. Satellite data

Eddy fields were analyzed using surface-velocity data provided by Ocean Surface Current Analysis Real-time (OSCAR) third-degree resolution of ocean surface currents (Ver. 1. PO.DAAC, CA, USA. Dataset accessed on 17 December, 2019 at https://doi.org/10.5067/OSCAR-03D01; Bonjean and Lagerloef, 2002) for 2001–2018. We calculated EKE from velocity, as follows:

$$EKE(x,y) \equiv \frac{1}{2}\left\langle (u(x,y,t) - U(x,y))^2 + (v(x,y,t) - V(x,y))^2 \right\rangle, \quad (1)$$

where, x, y, and t are zonal, meridional, and time components, respectively; u and v are zonal and meridional velocities at each grid and time, respectively; and U and V are temporal averages of zonal and meridional velocities for each grid, respectively. Large angle brackets denote temporal averages. Based on this definition, EKE includes the contributions of both meso-scale eddies and Rossby waves.

Surface Chl-*a* distributions were analyzed using GlobColour (http://globcolour.info) data developed, validated, and distributed by ACRI-ST (R&D), France (d'Andon et al., 2009; Maritorena et al., 2010). Data products of 25-km resolution and 8-d average were selected, with the level-three GSM01 (Garver-Siegel-Maritoren) merged model (Maritorena et al., 2002; Maritorena and Siegel, 2005). The merged data included data provided by three satellite sensors: SeaWiFS (Sea-Viewing Wide Field-of-View Sensor) on GeoEye's Orbview-2 mission, MODIS (Moderate resolution Imaging Spectroradiometer) on NASA's (National Aeronautics and Space Administration) Aqua mission, and MERIS (Medium Resolution Imaging Spectrometer) on ESA's (European Space Agency) ENVISAT (Environmental Satellite) mission. The period of study was again 2001–2018.

We considered five basins (NP, SP, NA, SA, and SI; Figure 1), focusing on mid-latitudes (15°–60°) because Chl-*a* concentrations are affected by sea ice at high latitudes and the accuracy of geophysical currents is poor at low latitudes due to the weak Coriolis force. The specific range of each basin was as follows: NP, 105°E–100°W, 15°N–60°N; SP, 140°E–70°W, 15°S–60°S; NA, 80°W–0°, 15°N–60°N; SA, 70°W–25E°, 15°S–60°S; and SI, 20°E–140°, 15°S–60°S.

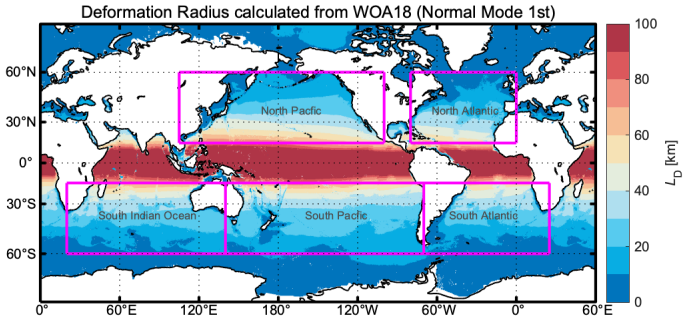

Figure 1. Locations of analyzed regions in five basins. Color indicates the internal Rossby deformation radius (L_{D}) calculated from World Ocean Atlas 2018 (see Section 2.3).

2.2. Horizontal scales of Chl-*a* distribution

Climatological time series of Chl-*a* concentrations at each grid point were calculated as means for 10-d intervals from January 2001 to December 2018, and anomalies in Chl-*a* concentrations were estimated. Correlation coefficients for each time-series of the Chl-*a* anomalies were plotted against distance for each grid point (see Figure S1 as an example), and mean correlation coefficients in each 10-km bin were calculated. The horizontal scale, D, was defined as the distance over which the mean correlation coefficient trends to e^{-1}. The scale may be regarded as a typical horizontal scale over which the spatial variation of Chl-*a* is synchronized (e.g., Ito et al., 2004).

We similarly calculated horizontal scales in the four directions (east (D_{E}), west (D_{W}), north (D_{N}), and south (D_{S})) from the central point in each grid cell, as horizontal scales of Chl-*a* would be expected to have a dominant direction due to factors such as solar radiation patterns, Rossby waves, and mean flow through the Gulf Stream and Kuroshio Current. The D_{E}–D_{W} and D_{N}–D_{S} means were defined as the horizontal scales in the zonal (meridional) direction, D_{m} or D_{z}, respectively. The ratio of horizontal scales, R_{D}, was calculated as follows:

$$R_D = \frac{D_z}{D_m} = \frac{(D_E + D_W)}{(D_N + D_S)}. \quad (2)$$

When $R_{\mathrm{D}} > 1$, the zonal (east–west) scale of Chl-*a* variation is thus greater than that in the meridional (north–south) direction.

2.3. Representative horizontal scales: Deformation radius and Rhines

scale

To estimate the scale of the internal Rossby deformation radius, we used data for temperature and salinity provided by the World Ocean Atlas 2018 (WOA18) with 0.25° horizontal resolution (https://accession.nodc.noaa.gov/NCEI-WOA18. Accessed on 19 February 2021; Boyer et al., 2018) for stratification calculations. The estimation method for the internal Rossby deformation radius was the same as that used by Kaneko et al. (2021); i.e., the potential density was calculated using means of temperature and salinity over each 0.25° grid. The Brunt–Väisälä frequency, N, was then calculated at each grid with the depth range of N being set to 0–4000 m. Based on the vertical distribution of N, we calculated the eigenvalue of the 1st vertical normal mode (e.g., Gill, 1982; Emery and Thomson, 2001; Figure S2) and the internal Rossby deformation radius (hereinafter "deformation radius"), L_{D}:

$L_D = \frac{c_{1st}(x,y)}{f(y)}$ (3)

where $c_{1\mathrm{st}}$ is the eigenvalue of the 1st vertical normal mode, and f is the inertial frequency at each latitude. The horizontal distribution of L_{D} is shown in Figure 1.

In addition to the deformation radius, another representative horizontal scale for geophysical fluids was also used—the Rhines scale (Rhines, 1975; 1977)—which is closely related to the horizontal scale in the meridional direction relative to two-dimensional turbulence on a plane, and thus closely related to eddy activity. There is some ambiguity in the definition of this scale (e.g., Eden, 2007), so we defined it as follows, based on a parameter related to the vertical structure of horizontal velocity:

$L_R = \left(\frac{2pS_e}{\beta}\right)$, (4)

where S_{e} is the representative eddy velocity scale for the estimation of the two-dimensional turbulence in the present study, defined as follows using the OSCAR surface velocity:

$S_e = \left\langle (u(x,y,t) - U(x,y))^2 + (v(x,y,t) - V(x,y))^2 \right\rangle^{\frac{1}{2}}$. (5)

The parameters and p in Eq. 4 are the planetary beta at each latitude and a coefficient for correction with the vertical distribution of horizontal representative velocity (i.e., the correction for two-dimensional turbulence), respectively. To estimate the representative velocity of two-dimensional turbulence, we used an exponential model for the vertical distribution of horizontal velocity, $u = u_0 \exp(-z/H)$ (Figure S3a), assuming an exponentially decreasing velocity in the vertical scale. The parameter p was then calculated, the product of which with the surface value (S_{e}) is equivalent to the vertical mean value. Specifically, p was estimated as follows:

$p = \frac{1}{4Hu_0} \int_0^{4H} \mathrm{udz}$, (6)

where u_0 is surface velocity. Assuming that the characteristic depth, H, would be 1000 m, with a mean basin depth of ~4000 m, Eq. 6 yields $p = 0.25$ (Figure

S3a). The eddy velocity scale for the Rhines scale was estimated using this parameter, and the surface velocity was obtained from OSCAR (Figure S3b).

To represent the relationships among D_{m}, L_{D}, and L_{R} in each basin as a horizontal map, an index, γ_{D} , was defined as the contribution of the deformation radius and Rhines scale to D_{m} as follows:

$$\gamma_{\mathrm{D}} = \frac{(D_{\mathrm{m}} - \mathrm{L_D})^2}{\left\langle (D_{\mathrm{m}} - \mathrm{L_D})^2 + (D_{\mathrm{m}} - \mathrm{L_R})^2 \right\rangle}. \quad (7)$$

$_{\mathrm{D}}$ approaches zero (one) when D_{m} is similar to the deformation radius (Rhines Scale).

2.4. Index for the effects of temporal-mean flow on Chl-*a* distribution

It was expected that intense background flows such as the Kuroshio Current and Gulf Stream would affect Chl-*a* distributions through advection in the downstream direction, even in high meso-scale eddy activity, so we used the value of R_{D} as an index of the relationship between mean flow and isotropic eddy motion. Assuming a typical radius of an isotropic eddy, r, the timescale of the long-term temporal-means of velocity, T_{m}, and eddy, T_{e}, were calculated as follows:

$$T_{\mathrm{m}} = 2r/U, \text{ or } 2r/V \quad (8)$$

$$T_{\mathrm{e}} = 2\ r/S_{\mathrm{e}}. \quad (9)$$

The ratio of timescales was used as an index of the influence of mean flow on the isotropic eddy effect, as follows:

$$I_{\mathrm{t}} = T_{\mathrm{e}}/T_{\mathrm{m}} = \ U/S_{\mathrm{e}}, \text{ or } \ V/S_{\mathrm{e}}, \text{ or } \ S_{\mathrm{m}}/S_{\mathrm{e}}, \quad (10)$$

where U, V, and S_{e} are as defined above. S_{m} is the mean surface velocity. If I_{t} 1, the timescale due to isotropic eddy motion is far longer than that caused by mean flow, and it would be expected that the horizontal distribution of Chl-*a* would be stretched in the direction of mean flow. Conversely, R_{D} would be expected to be near 1 when I_{t} 1. The relationship of R_{D} with EKE under large-I_{t} conditions is discussed in Section 3.2.

3 Results

3.1. Horizontal distributions of Chl-*a*

Long-term (18 yr) average Chl-*a* concentrations display a well-known contrast in the meridional direction, with lower concentrations in subtropical (lower latitude) regions and higher concentrations in subarctic (higher latitude) regions (Figure S4). At latitudes of 30°–50°, basin-scale zonal gradients of Chl-*a* concentration are indicated in the SA and SP, with higher concentrations in western than eastern regions (Figure 2).

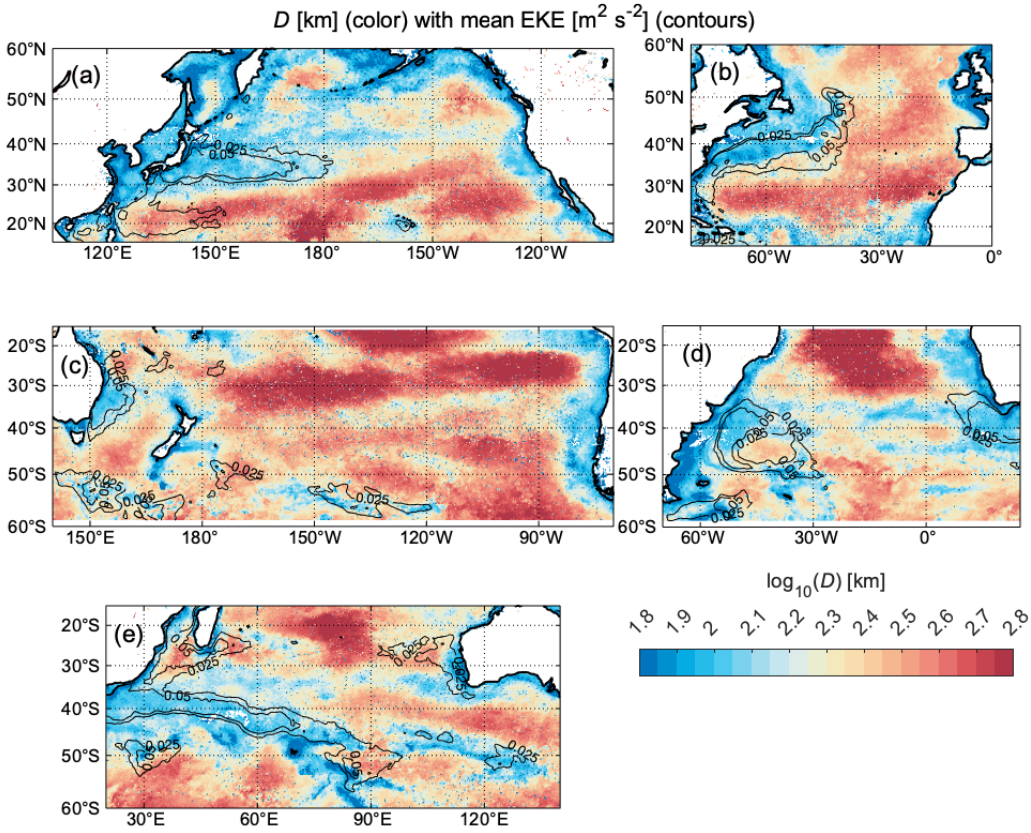

Figure 2. Maps of the horizontal characteristic scale of chlorophyll *a*, *D* (color), in (a) the North Pacific, (b) the North Atlantic, (c) the South Pacific, (d) the South Atlantic, and (e) the South Indian Ocean. Contours denote the eddy kinetic energy, EKE.

The horizontal distribution scale of Chl-*a*, *D*, shows a similar variation between zonal directions, especially in latitudes of 30°–50°, with another in the meridional direction (Figure 2). *D* is relatively large (>500 km) in the subtropical (below ~30° latitude) and eastern regions of each basin. *D* is smaller in the subarctic and western regions of each basin, at a scale of a few hundred km, and is also small (~100 km) in coastal regions. By comparing *D* with EKE it is clear that *D* is reduced in regions of high EKE, especially in the Kuroshio Extension (30°N–40°N, 140°E–180°; Figure 2a), Gulf Stream (30°N–40°N, 50°W–70°W; Figure 2b), East Australian Current (30°S–40°S, 150°E–160°E; Figure 2c), Brazil–Malvinus Confluence Region (35°S–45°S, 40°W–60°W; Figure 2d), and the region from the Agulhas Current to the Agulhas Return Current (30°S–45°S,

25°E–70°E; Figure 2e).

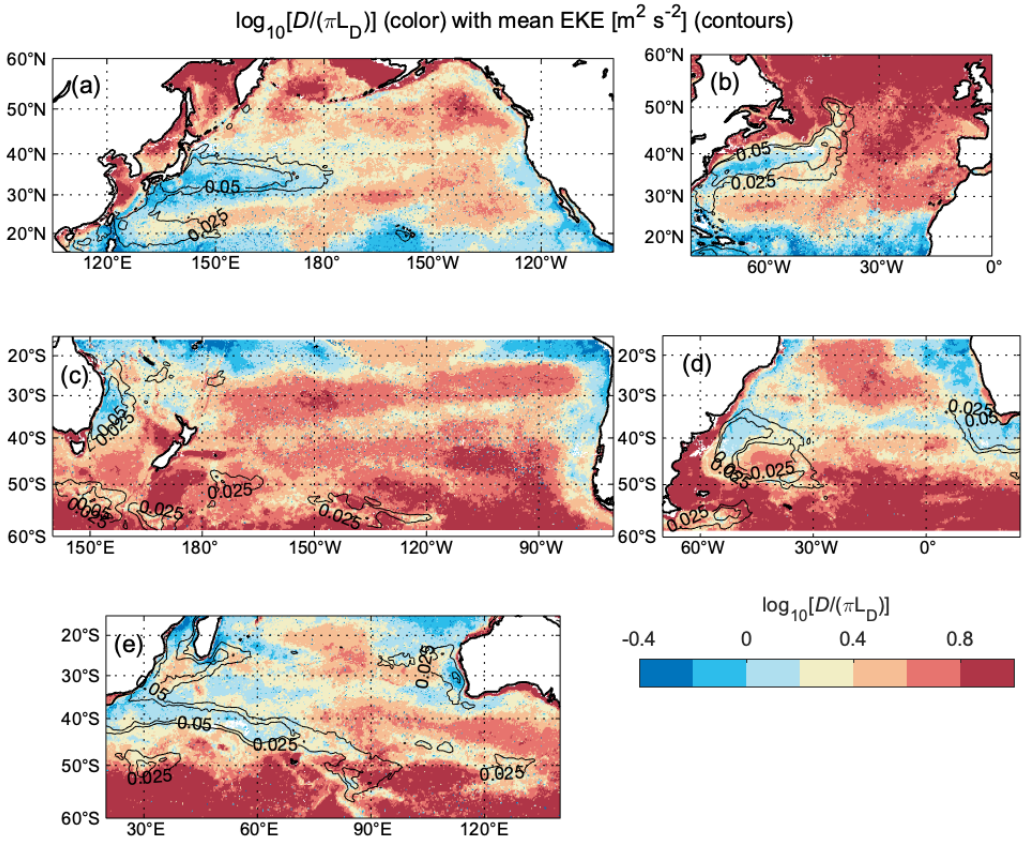

Figure 3. Maps of the normalized horizontal characteristic scale of chlorophyll *a* by the internal Rossby deformation radius, $D/\ L_{\mathrm{D}}$ (color), and eddy kinetic energy (contour) in each basin. (a)–(e) are same as Figure 2.

The horizontal scale is similar to the deformation radius in regions where EKE > 0.025 m^2 s^{-2} and latitude $> 25°$ ($D/\ L_{\mathrm{D}}$ ~1, Figure 3), suggesting a close relationship between Chl-*a* distribution and the activity of meso-scale eddies in these western boundary regions. The dependence of the ratio of horizontal scale and deformation radius on EKE is illustrated by a plot of $D/\ L_{\mathrm{D}}$ vs. EKE, with a calculated average $D/\ L_{\mathrm{D}}$ value of 0.02 m^2 s^{-2} in each bin for the five basins (Figure 4). Bin-averaged $D/\ L_{\mathrm{D}}$ ratios generally shows a monotonical decrease with increasing EKE, converging to ~1 at an EKE of 0.15 m^2 s^{-2} in each basin. Least-squares fitting was applied to the average of each 0.02 m^2 s^{-2} bin (Figure 4) with an exponential decay model:

$$\log_{10}\ [D/\pi L_D] = A\ \exp\left(-EKE/k_e\right), \quad (11)$$

where A is amplitude and k_e is the e-folding scale relative to EKE. The e-folding scale, k_e, varied from 0.04 to 0.11 $m^2\ s^{-2}$ in each basin (Figure 4). Considering that the scale of the deformation radius in these western boundary regions was 30–50 km (Figure 1), the scale of D convergence was 90–150 km, consistent with that of mesoscale eddies (e.g., Chelton et al., 2011b). This suggests that D could be regarded as the representative of radius of mesoscale eddies in regions of remarkable eddy activity.

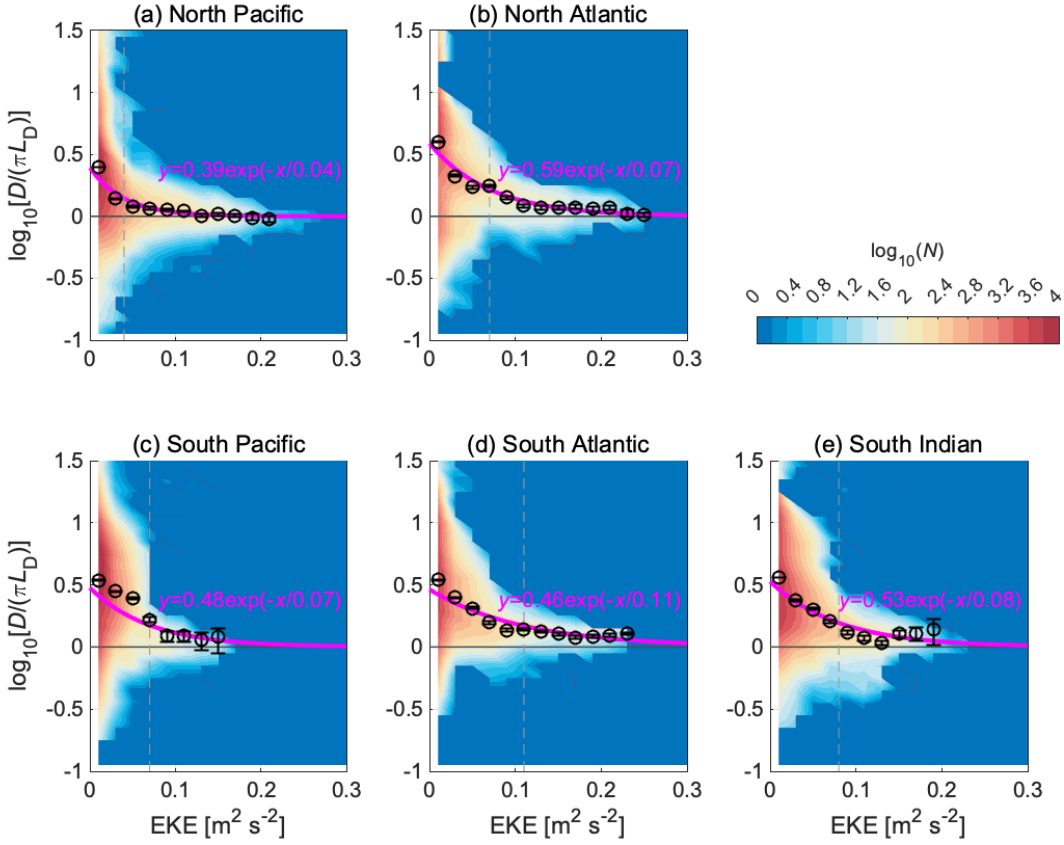

Figure 4. Frequency distribution of the normalized horizontal characteristic scale of chlorophyll a by the Rossby's internal deformation radius, $D/\ L_D$ (y-axis), to the eddy kinetic energy (EKE, x-axis) in each basin. (a)–(e) are same as Figure 2. Circles are mean D at each 0.02 $m^2\ s^{-2}$ bin of EKE with 95 % confidence interval. Magenta line indicates a least square fitting curve defined by the equation 11.

3.2. Anisotropy in Chl-*a* distribution

Characteristics of the horizontal scale, D, in relation to all directions were described in Section 3.1, but the distribution of Chl-a would be expected to have a dominant direction due to factors such as advection with background flows (Section 2.2). Therefore, using the ratio of the zonal scale of Chl-a (D_z) to the meridional characteristic scale (D_m), R_D, we replotted features of the distribution of anisotropy (Figure 5). The zonal characteristic scale is generally larger than the meridional scale (indicating anisotropy), especially in eastern and subtropical regions in each basin. In the SA and SP, zonal directionality is evident at higher latitudes (>40°S). In these regions where R_D is » 1, the zonal characteristic scale, D_z, sometimes reaches 500 km (Figure S4), while the meridional characteristic scale, D_m, is 200–300 km (Figure S5). In contrast, R_D tends to be near 1 (indicating isotropy) in regions with EKE > 0.025 m^2 s^{-2} (Figure 5). This suggests that horizontal distribution of Chl-a tends to be isotropic in regions with high EKE, such as western boundary regions.

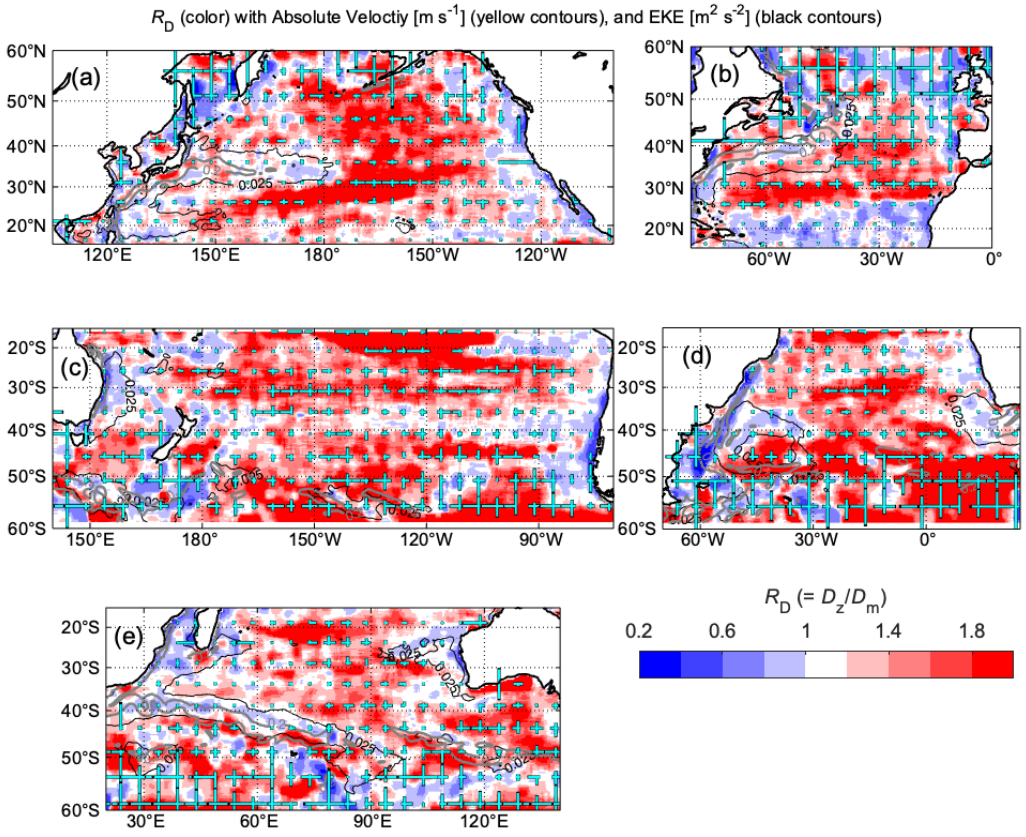

Figure 5. Ratio (R_D) of the horizontal characteristic scale in the zonal direction,

D_z, to that in the meridional direction, D_m, in each basin. (a)–(e) are same as Figure 2. Cyan crosses denote horizontal characteristic scale of chlorophyll a on each direction (east, west, north, and south). Black (grey) contours denote the eddy kinetic energy, EKE (absolute velocity).

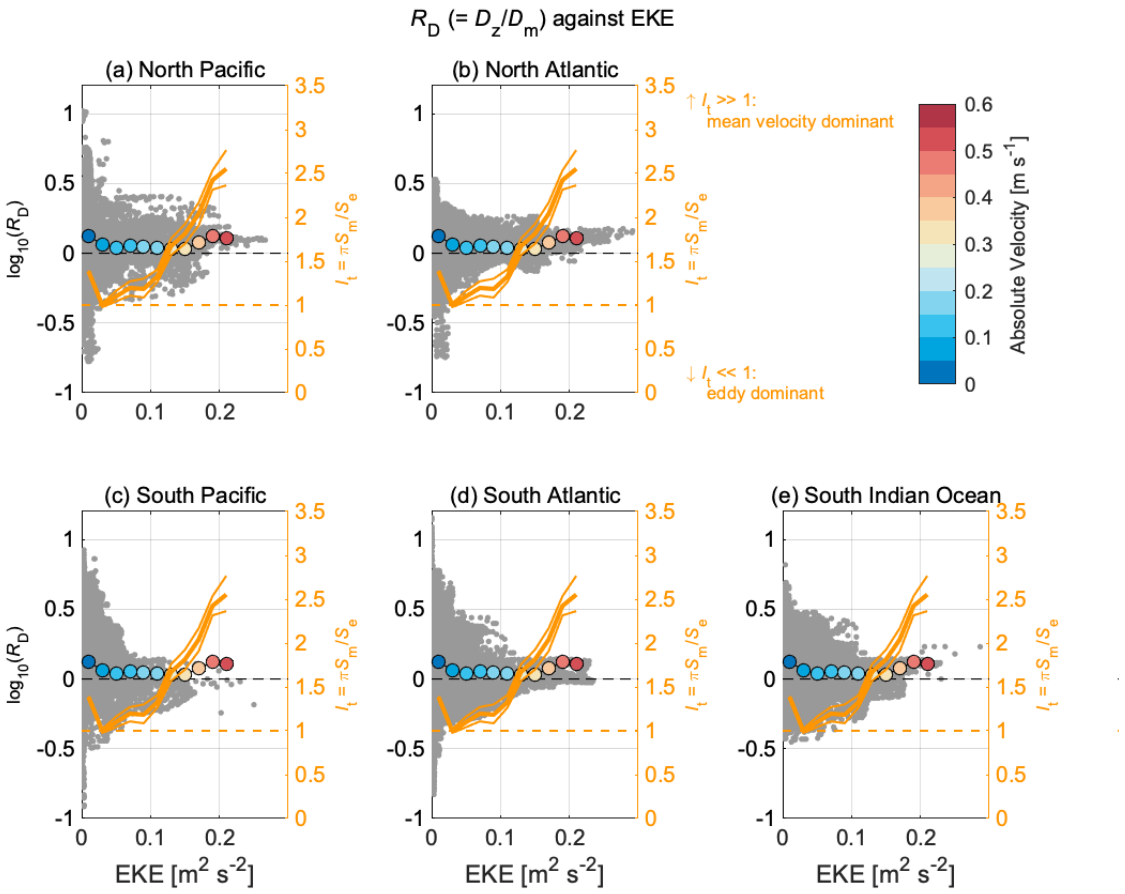

Figure 6. Plots of the ratio of the horizontal characteristic scale in the zonal direction to that in the meridional direction (R_D, y-axis) to the eddy kinetic energy (EKE, x-axis). Circles denote the mean of R_D in each 0.05 m^2 s^{-2} bin of EKE, and color in the circles represents mean velocity of each bin. Orange lines show the index of an effect of mean velocity in relation to that of eddy, I_t, considering transit time due to the former and time to make one round by the latter (see section 2.3). Thin lines denote 95 % confidence interval.

The distribution of R_D generally converges to 1 with increasing EKE (Figure 6). The average R_D of 0.02 m^2 s^{-2} (Figure 6) in the SP and SA also indicates isotropy. In contrast, however, such convergence is unclear in the NP, NA, and

SI, with R_D increasing with EKE. In the latter three basins, a high temporal-mean velocity (>0.4 m s^{-1}; Figure 6) is evident in higher EKE ranges (>0.15 m^2 s^{-2}; Figure 6), suggesting that high mean flows affect the distribution of R_D in these basins. The time-scale ratio index of I_t (Section 2.4) between eddy and mean flows (larger values indicate stronger influence of the mean flow) in these basins display an increasing trend with EKE (Figure 6). The zonal distribution of R_D with respect to index values (U/S_e) in the three basins indicates that R_D frequently exceeds 1 in the range of $U/S_e > 5$, suggesting that strong zonal velocity distorts the Chl-*a* distribution in the zonal direction (Figure 7). Similarly, R_D tended to be <1 in the range of $V/S_e > 5$ (Figure 7), indicating that strong meridional velocity distorts the Chl-*a* distribution in the meridional direction within the three basins, even in regions of high eddy activity.

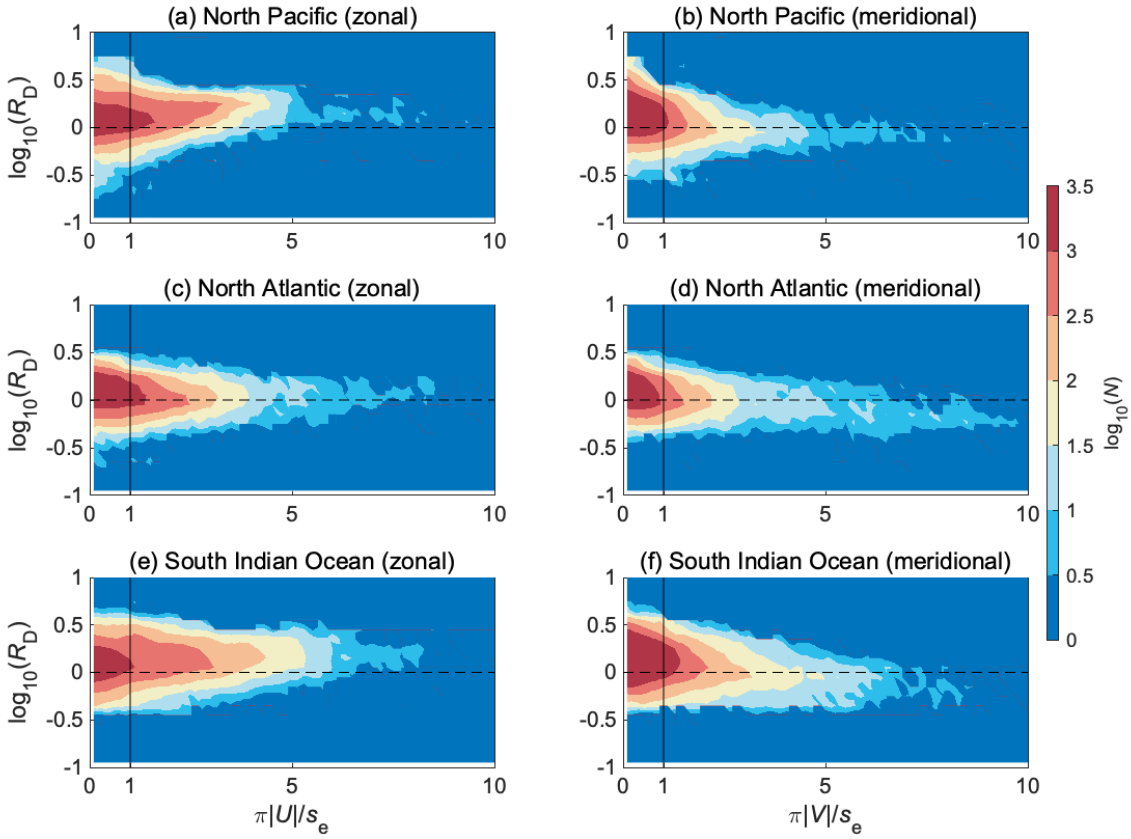

Figure 7. Plots concerning the ratio of the horizontal characteristic scale in the zonal direction to that in the meridional direction, R_D (y-axis), against the index of the timescale, I_t (x-axis), in (a) and (b) the North Pacific, (c) and (d) the North Atlantic, and (e) and (f) the South Indian Ocean. Left (right) column

denotes in the case of $I_t = U/S_e$ (V/S_e).

R_D exceeds 1 (indicating domination along the zonal direction) in some western boundary regions including the south of Japan (~32°N, 130°E–140°E; Figure 5a), the Gulf Stream (~38°N, 70°W–80°W; Figure 5b), and the Alaskan stream (52°N–54°N, 170°W–160°W; Figure 5a). In the SI, $R_D > 1$ in the region from the Agulhas Current to the Agulhas Return Current (~35°S, 20°E–30°E and 40°S–50°S, 30°E–80°E, respectively; Figure 5e). R_D values below 1 (domination along the meridional direction) occur near the Luzon Straits in the NP (20°N–25°N, ~120°E; Figure 5a). In the NA, this occurs in the Labrador Current region (50°N–60°N, 60°W–50°W; Figure 5b). These results are consistent with occurrence of strong mean currents (Figure 5).

3.3. Comparisons with the Rhines scale

Above, we focused mainly on regions where eddies are active, such as western boundary regions. However, distribution scales of Chl-*a* larger than L_D are observed in eastern and subtropical regions in each basin (Figure 3), where the velocity amplitude of mean flow is not large enough to distort the Chl-*a* distribution. The propagation of Rossby wave may enlarge the zonal distribution of Chl-*a*. We compared the latitudinal distribution with horizontal scales of Chl-*a*, D_m, and D_z, to the Rhines scale, L_R (Figure 8) and L_D, for cases of weak and intense EKE. L_D has a decreasing trend with increasing latitude, whereas the latitudinal distribution of L_R is relatively constant because the increasing trends with decreasing latitude are balanced for planetary and S_e (Figure S3b). As a result, although $L_R > L_D$ at latitudes above 25°, the magnitudes of L_R and L_D are reversed at subtropical latitudes below 25° in the weak EKE region (Figure 8a).

In the weaker EKE range, D_m (meridional direction) displays two maxima in the frequency distribution (Figure 8a) at ~100 km and ~200 km at all latitudes, except for 20°–30°. One maximum centered around ~100 km for the horizontal scale is somewhat smaller than L_R, whereas the other at ~200 km is similar to L_R. The mean D_m at each latitude (Figure 8a) is also similar to L_R. As an exception the frequency distribution of D_m in the 15°–35° region indicates a larger scale (>~300 km) than L_R, with an increase in mean D_m. This large D_m is likely affected by the D_m at the center of each basin in the latitudinal range, especially in the Southern Hemisphere (Figure S5); however, the scale of D_m is far smaller than the external deformation radius O (10^3 km) at mid-latitudes, assuming the water depth is ~4000 m. In contrast, in the larger EKE range (Figure 8b), D_m generally ranged around L_D, with the mean D_m at each latitude (Figure 8b) generally being $< L_R$ and showing similarity with L_D at latitudes of 30°–40° where high eddy activity associated with the western boundary current and its extensions occur (Figure 4). An exception is the 20°–30° latitude region where D_m tends to be larger than L_D.

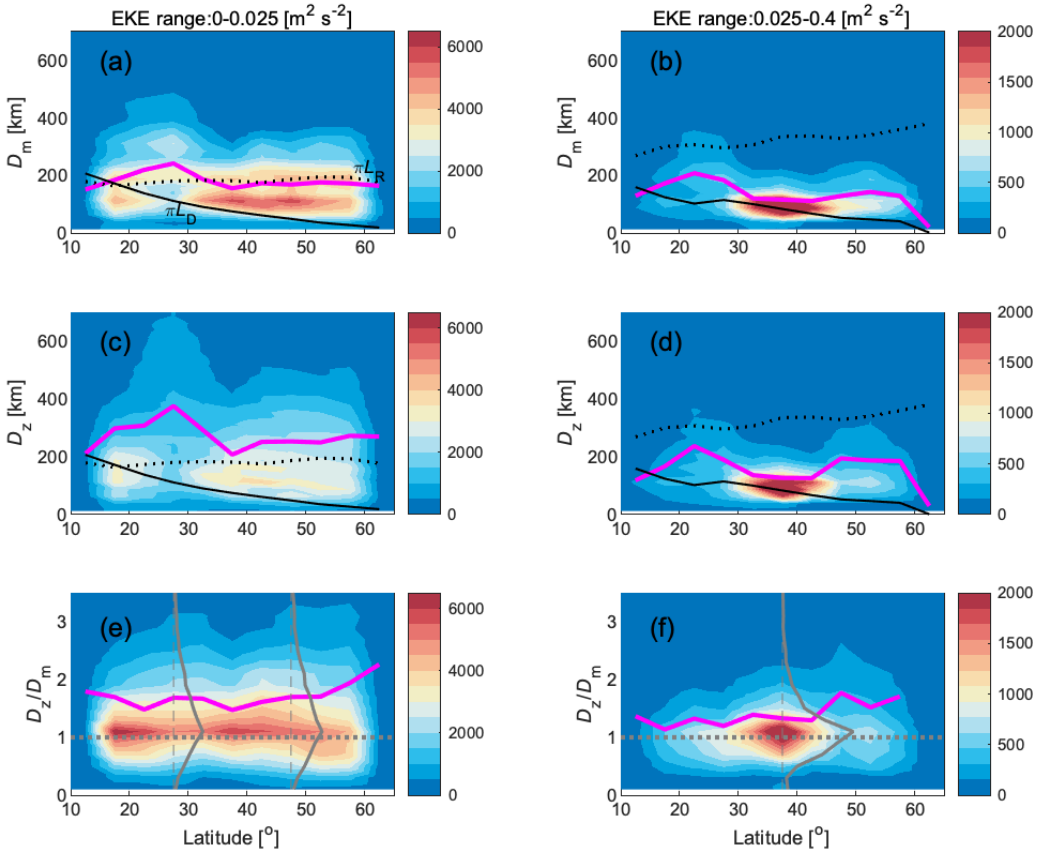

Figure 8. Latitudinal distribution (frequency is shown as color) of the horizontal scales in the eddy kinetic energy, EKE, of 0.00–0.05 (0.05–0.40) m^2 s^{-2} in the left (right) column. (a) and (b) regarding the horizontal characteristic scale in the meridional direction (D_m), (c) and (d) regarding the horizontal characteristic scale in the zonal direction (D_z). (e) and (f) the ratio of the horizontal characteristic scale in the zonal direction to that in the meridional direction. Magenta line indicates the mean value at each latitude (five-degrees width). Gray solid lines in (e) and (f) denote histogram at certain latitude as examples (broken lines, and dashed line show zero level at each latitude, and $D_z/D_m = 1$, respectively).

In relation to D_z (zonal direction), the frequency distribution (Figure 8c, d) has similar characteristics to those of D_m in the case of higher EKE (Figure 8b). However, at lower EKE (Figure 8c) it is clear that (1) the larger maximum in the frequency distribution around L_R is not as pronounced as that for D_m; (2) the peak of the frequency distribution of D_z (Figure 8c) decreases with increasing

latitude, in contrast to the weak latitudinal dependence of D_m; and (3) the frequency distribution of D_z has a longer tail than that of D_m at each latitude.

The contrasting latitudinal distribution between D_m and D_z at lower EKE (Figure 8a, c) suggests that the enlargement of eddy activity owing to the cascade of two-dimensional turbulence in the meridional direction may be restricted at a certain scale (such as the Rhines scale); hence, the meridional characteristic scale of Chl-*a* would also be restricted in such regions. In contrast, because the zonal direction is the main direction of propagation of the long Rossby waves in a flat basin, D_z would be unrestricted by the Rhines scale. Although the vertical distribution of speed relating to eddy activity was assumed to decrease exponentially with increasing depth (Figure S3a), and p was used for the Rhines scale (Section 2.3), the weak latitudinal dependence of D_m likely indicates that the planetary effect on the meridional scale restriction would also affect the Chl-*a* distribution. The longer-tail distribution of R_D ($= D_z/D_m$) at each latitude of low EKE leads to an average D_z/D_m ratio of >1 (R_D ~1.5) at low EKE (Figure 8e), suggesting that such phenomena with longer structures in the E–W direction than in the N–S direction would occur frequently in the low EKE region. In contrast to the region of lower EKE, such differences concerning latitudinal dependence between D_m and D_z are not clear at higher EKE (Figure 8b, d). Moreover, in the high-EKE range, the distribution of R_D at each latitude is closer to a symmetrical bell-shaped distribution with R_D of ~1 (Figure 8d), which is consistent with the structure of meso-scale eddies.

We mapped the index of $_D$ (Section 2.3) for each basin to confirm where D_m is nearer the deformation radius or the lines scale (Figure 9). In western parts of the basins with high-eddy-activity regions (EKE > 0.025 m^2 s^{-2}), $_D$ was generally <0.5, suggesting a larger influence of the deformation radius (Figure 9). In contrast, in the eastern part (except near the coast) and at the subtropical latitudes of each basin, $_D$ was frequently >1, suggesting that the horizontal distribution of Chl-*a* was closer to the Rhines scale (Figure 9). Between these extreme regions, especially at 30°–50° latitude near the center of each basin, $_D$ ranged from 0.5 to 1.0, indicating that D_m is possibly defined by the Rhines scale in these intermediate regions between the western and eastern parts of each basin such as the region of 40°N–50°N, 160°E–170°E in the NP (Figure 9a).

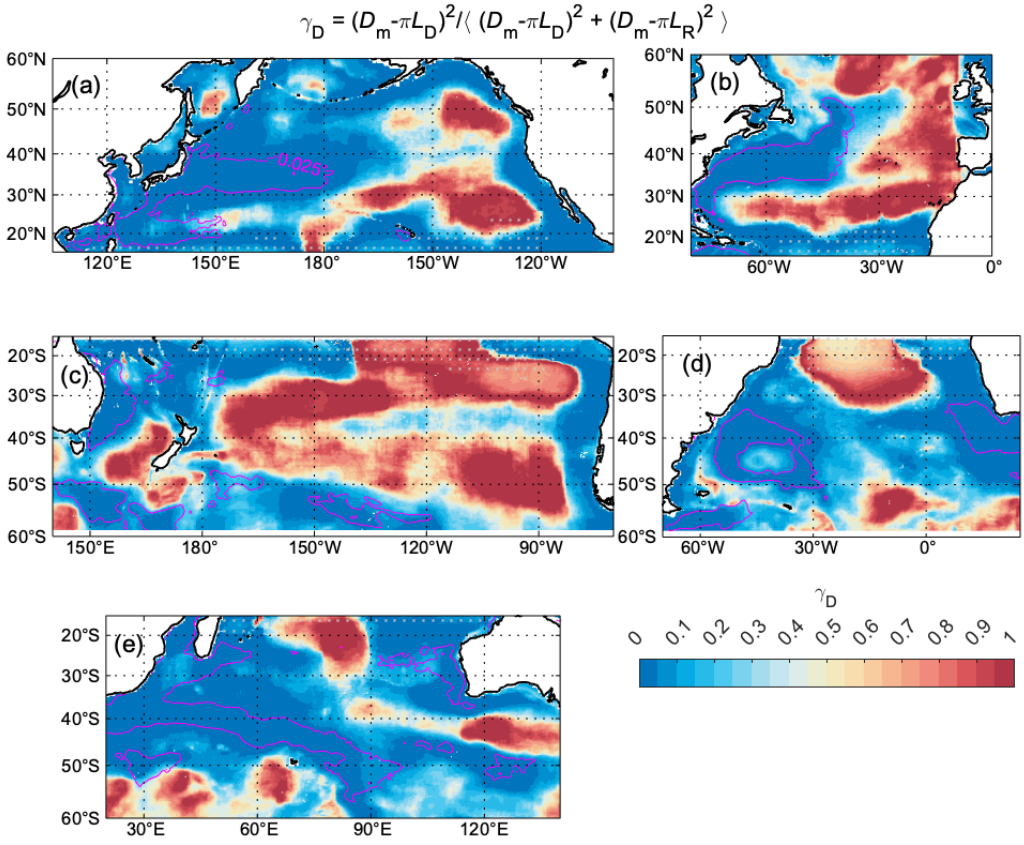

Figure 9. Maps concerning relationships of the meridional characteristic scale regarding chlorophyll *a*, D_m, with other representative scales (derived from the equation 7) in each basin. (a)–(e) are same as Figure 2. Magenta contours denote the eddy kinetic energy.

4 Discussion

4.1. Distribution of Chl-*a* in regions of high eddy activity

We compared the horizontal distribution of D with the level of EKE (deviations from long-term means) in the five basins. In all basins D converges to L_D with increasing EKE (Figure 4). The scale of D is ~100 km at latitudes of 30°–50°, including high-eddy-activity regions (Figure 2), which is consistent with mesoscale eddies (e.g., Chelton et al., 2011b), although the deformation radius has latitudinal dependence. The ratio of the meridional scale to the zonal scale, R_D, tends to converge to 1, except for in regions where temporal-mean flow has a large effect on eddies (Figures 6 and 7). In regions of high eddy activity, the

horizontal distribution of Chl-a, and hence phytoplankton, are considerably affected by meso-scale eddies, with distributions having near-isotropic structures (with local anomalies). Previous studies (e.g., McGillcudy, 2016) have indicated various physical processes related to meso-scale eddies that can make the Chl-a distribution aggregated and isotropic within/around eddies as mentioned in the Introduction. It is unclear which effects have the greatest control on the isotropic distribution; i.e., whether the meso-scale eddies themselves become the field of isotropic production, such as eddy pumping associated with isopycnal heaving within eddies, and/or whether the eddies convert the background distribution of Chl-a to their own scale through disturbing the Chl-a gradient of the background field via horizontal stirring along eddy peripheries. As the horizontal resolution of Chl-a data (~25 km) is limited, the effects of local blooms at smaller scales cannot be evaluated. However, the contours of EKE and those of the long-term mean Chl-a concentration (Figure 2) do not necessarily match, so it is plausible that horizontal stirring reduces the ambient gradient of Chl-a. Eddy stirring is the predominant mechanism influencing Chl-a distributions (Gaube et al., 2014). For western boundary current regions and their extensions, such as the Kuroshio Current, Agulhas Current, and Brazil–Malvinas Confluence, McGillicuddy (2016) suggested the effects of eddy pumping and horizontal uptake of high-Chl-a water from the coast due to eddies in addition to the eastern boundary current systems, including the California, Peru–Chile, and Benguela currents. The mapping shown here is consistent with the results of Gaube et al. (2014) and McGillicuddy (2016).

4.2. Regional differences in convergence sensitivity of Chl-a distribution vs. EKE

We found large horizontal scales of Chl-a distribution in the eastern parts and subtropical latitudes of each basin where eddy activity is low. However, this does not mean that the effects of meso-scale eddies on Chl-a variability in these regions are small. We also need to consider that the sensitivity of the Chl-a variations to EKE may vary depending on local features; in the NP, for example, more rapid convergence of $D/\ L_{\mathrm{D}}$ relative to EKE than in the other basins is indicated in Figure 4. This means that the horizontal distribution of Chl-a in the NP may be more sensitive to eddy activity than in the other basins. Such characteristics may also occur in smaller areas within each basin. Therefore, we examined more individual differences in e-folding magnitude relative to EKE, k_{e}, for sub-areas within each basin (Figure 10). We defined sub-areas that had one-tenth the length of parental areas analyzed (Figure 1) by latitude or longitude. Each sub-area was half-overlapped (for example, sub-area 1 in the NP is 105°E–120.5°E, 15°N–19.5°N; sub-area 2 is 112.75°N–128.25°N, 15°N–19.5°N), and calculated the e-folding value for each sub-area. Here, k_{e} was calculated using the least-squares fitting of the exponential-decline model (Eq. 11).

We found that k_{e} tends to be higher in western boundary regions where eddy activity is high, and lower in eastern basin areas (Figure 10). To confirm this, we replotted k_{e} as a function of normalized longitude within each basin (normalized

longitude of 0 indicates the western boundary and 1 the eastern boundary; Figure 11a). The mean k_e value was higher in the western part of the basin (0–0.2, Figure 11a) than that in the eastern part where EKE was relatively low, except for very near the eastern boundary (0.6–0.8, Figure 11a). This means that in the eastern part of each basin, sensitivity to EKE was high despite the horizontal scale of Chl-a (D) being larger than the deformation radius (Figures 3 and 9), and the weak mean EKE level (Figure 11b). This suggests that existence of meso-scale eddies may also have a large impact on local Chl-a activity in the eastern part of the basin, as observed in the western boundary region.

An example of the importance of such meso-scale eddies on primary production is provided by the eastern NP, which is characterized by high nutrient and low Chl-a concentrations (e.g., Martin et al. 1989) with distinctive eddies (Crawford 2002; 2005, Ueno et al., 2009; 2010). Previous observations indicate that meso-scale eddies may affect primary production through transport of iron from coastal regions into the Alaska gyre (e.g., Johnson et al., 2005; Whitney et al., 2005). The high sensitivity of Chl-a distributions to eddy activity in the eastern part of the NP is consistent with this. Other areas with high sensitivities (small k_e), including subtropical latitudes of the eastern NA boundary, subtropical latitudes of the western boundary and mid-latitude central region of the SA, and the southwestern region of the Australia region (Figure 10), also seem to coincide with the areas of iron limitation (Browning et al., 2017). The high sensitivity of D in the lower EKE range in these regions may be related to such micro-nutrient limitation and its supply through transport by the nonlinear meso-scale eddies, although further studies are needed.

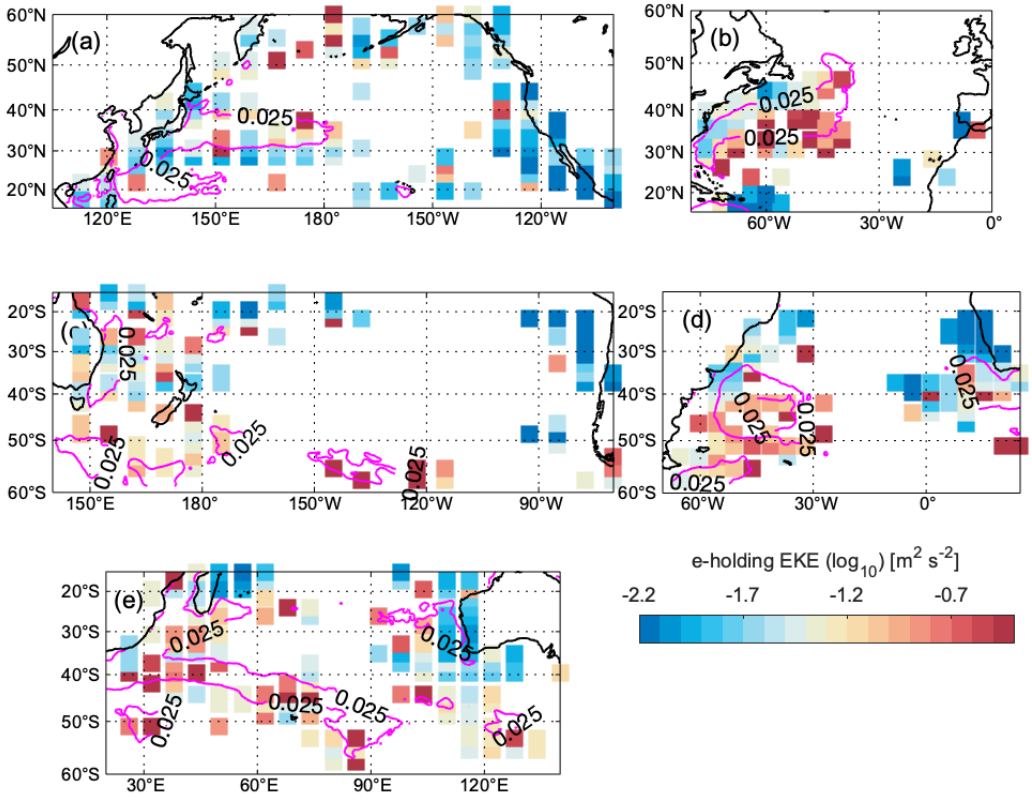

Figure 10. Detailed horizontal distribution of the e-holding magnitude of the eddy kinetic energy, k_e, (see the equation 11) in each basin. Magenta contours denote the eddy kinetic energy.

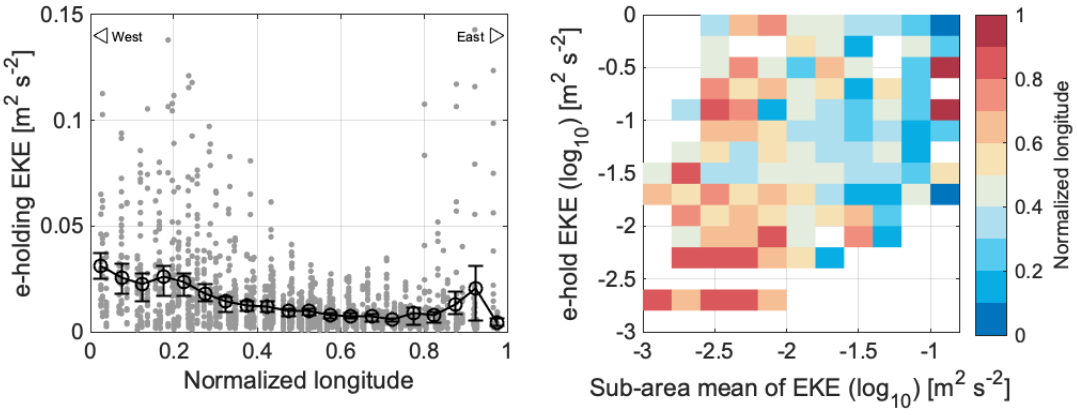

Figure 11. Plots of the e-holding magnitude of the eddy kinetic energy, k_e, against (a) the normalized longitude of each sub-area in each basin, and against (b) the sub-area mean of the eddy kinetic energy. Circles with error bars in (a) are mean of each 0.04 sub-grid (x-axis direction) with 95% confidence intervals. Colors in (b) denotes average of the normalized longitude.

4.3. The larger horizontal scale of Chl-a in subtropical regions

Here we consider the larger horizontal scale of Chl-a distribution than the deformation radius in low-EKE regions, focusing on subtropical regions (Figures 3 and 9). Specific areas with large D_z were estimated for each basin (Figure 12a), partly overlapping areas investigated by Chelton et al. (2011a), who recorded a mean radius of meso-scale eddies in the southeastern Pacific (SEP; 22°S, 130°W–80°W) of 110 km. This radius is comparable with L_D at this latitude (Figure 8a, and c), but far smaller than mean D_z over the box region in the SP (~1070 km). Therefore, in addition to the nonlinear meso-scale eddies (likely having large impact on Chl-a distributions; Section 4.2), larger spatial phenomena such as Rossby waves may affect the horizontal distribution of Chl-a (Cipollini et al., 2001; Uz et al., 2001; Seagel, 2001; Killworth et al., 2004). Chelton et al. (2011a) indicated that nonlinear meso-scale eddies with a similar westward propagation to that of long linear Rossby waves in these areas may cause the Chl-a anomalies to lag the passage of meso-scale centers. However, Chelton et al. (2011a) also noted some difficulty concerning the determination of features of Chl-a variability based on their zonal-wavenumber–frequency spectrum, compared with that of sea-surface height (e.g., Figure 5 in Chelton et al., 2011a). We therefore considered Rossby waves further.

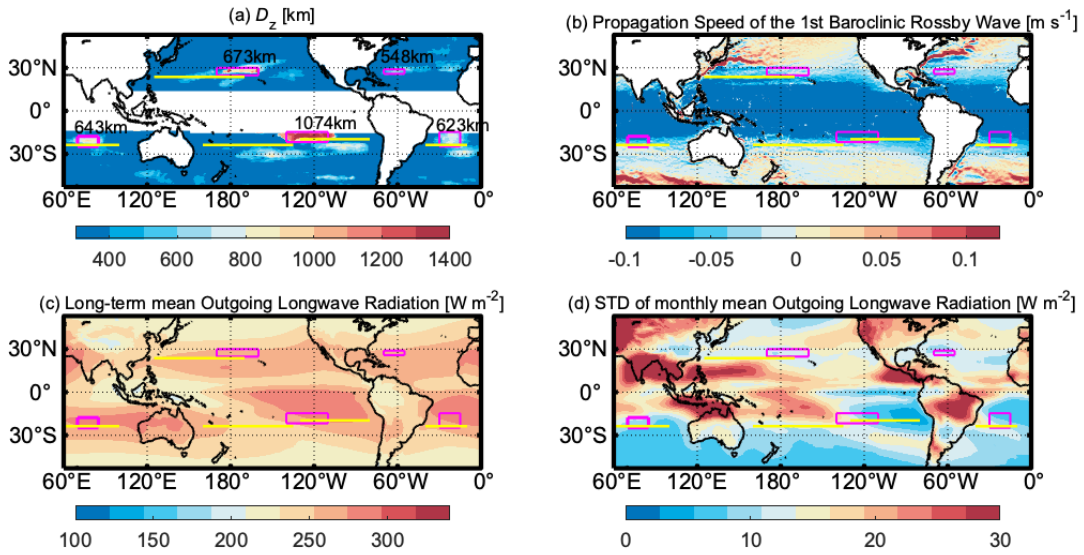

Figure 12. Distribution of (a) horizontal characteristic scale of chlorophyll *a* in the zonal direction, (b) propagation speed of long Rossby wave (1st baroclinic mode), (c) long-term mean of longwave radiation, and (d) standard deviation of monthly mean longwave radiation. The yellow lines denote the zonal sections for the investigation of the zonal wavenumber-frequency spectra of filtered sea surface height in Chelton et al. (2011a).

We checked that these box areas (Figure 12) correspond to the regions where Rossby waves (with a first mode of vertical structure and far longer zonal wavelength than the deformation radius) could propagate westward (Figure 12b; see text S1 for the calculation of propagation speed). These areas correspond to those with high average outgoing longwave radiation (Hai-Tien Lee, and National Oceanic and Atmospheric Administration (NOAA) Climate Data Record (CDR) Program, 2011; doi:10.7289/V5SJ1HH2; Figure 12c) with small seasonal variations (Figure 12d). Because high out-going long-wave radiation indicates weak atmospheric convection, high and stable long-wave radiation in these regions of large D_z would imply that the effect of short-term atmospheric disturbances on the characteristics of the Chl-*a* distribution (e.g., Lin et al., 2003; Babin et al., 2004), such as tropical cyclones with horizontal scales of hundreds to 1000 km, would be small in these areas. We also mapped a longitude–time plot of the deviation of Chl-*a* concentration from the zonal mean at each time for each box of Figure 12a (Figure 13). Figure 13 indicates that in addition to a "pockmarked" distribution, larger E–W anomalies of similar scale with average D_z also seem to propagate westward with the propagation speed of long Rossby waves (Text S1) in each basin. This is consistent with an effect of Rossby waves on Chl-*a* variations (e.g., Cipollini et al., 2001). Although the contributions of these phenomena to the horizontal scale of Chl-*a* distributions are unclear, the

diversity of factors defining the spatial scale of Chl-a may affect the broader distribution of D_{m} and D_{z} at subtropical latitudes (20°–30°) with low EKE more than at other latitudes (Figure 8a, c).

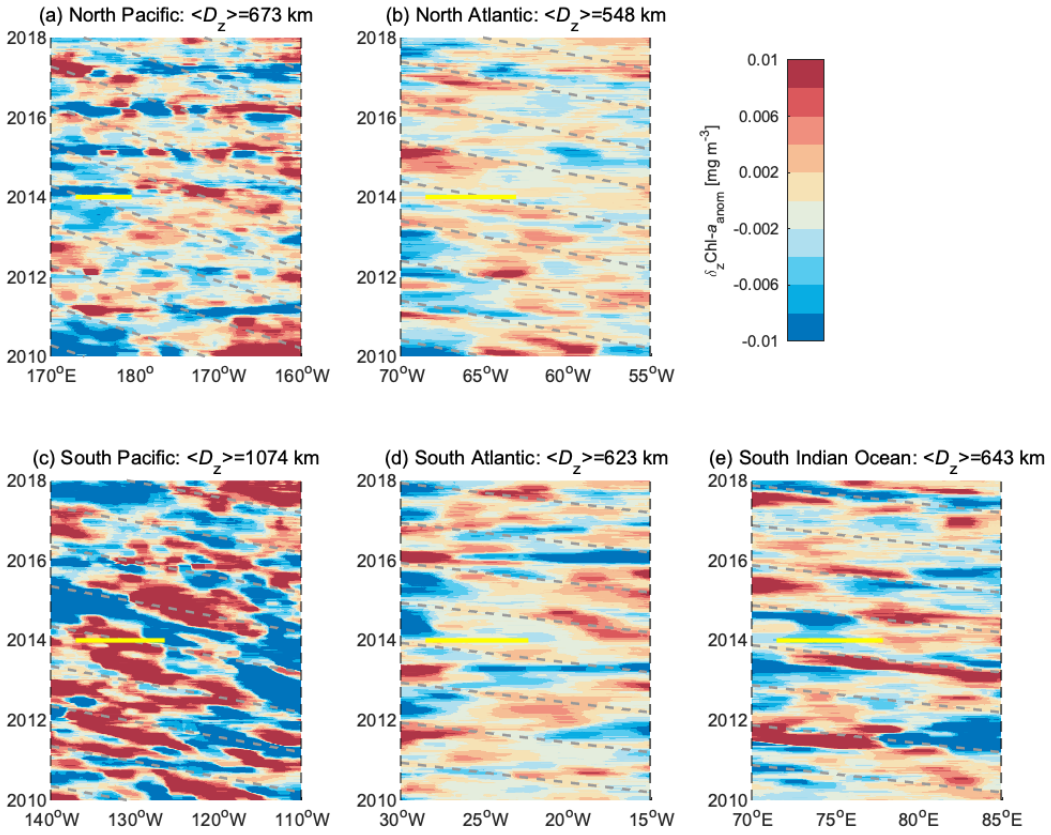

Figure 13. Longitude–time of chlorophyll a anomaly. Zonal average at each time is subtracted. Yellow lines denote the scale of the regional average of D_{z}. Broken lines indicate propagation speed of the long Rossby wave (see Text S1).

5. Concluding remarks

Wider regions in each ocean basin were investigated than those covered by Gaube et al. (2014), and a Eurlerian perspective was adopted. The geophysical contrast of the horizontal distribution of Chl-a, especially in the zonal direction, was emphasized; with a smaller scale of ~100 km in western boundary regions of high eddy activity and a larger scale of several hundreds to a million km in eastern and subtropical parts of each basin. The latitudinal distribution of Chl-a in the meridional (N–S) direction (D_{m}) in regions of low EKE (0–0.025

m^2 s^{-2}) does not have a clear latitudinal dependence (as exhibited by the deformation radius), and its mean value is near L_R. The zonal scale (D_z) tends to be larger than the meridional scale (D_m) in these regions. This suggests that the distribution of Chl-*a* in regions of weak EKE, such as the eastern and central subtropical region of the basins, is affected by phenomena of planetary scales (including Rossby waves) and is larger than the deformation radius. It should be also noted that in the eastern and subtropical parts of each basin, the sensitivity of the horizontal distribution of Chl-*a* to eddy activity tends to be higher than that in western boundary regions, indicating the importance of meso-scale eddies in these areas.

The geographical distribution of Chl-*a* associated with temporally changing eddy activity, including both meso-scale eddies and Rossby waves, aids our understanding of the contributions of eddies to basin-scale Chl-*a* variations. Long-term eddy variations related to western boundary currents (e.g., Qiu and Chen, 2011) may also impact Chl-*a* distributions in western boundary regions (e.g., Kouketsu et al., 2016), so investigation of decadal variations of D would be helpful. The present results also indicate the importance of examining the impact of eddy activity on the Chl-*a* distribution from multiple perspectives, especially in the intermediate region between the eastern and western boundary regions. A variety of eddy activities may affect the distribution and long-term variability of Chl-*a* in the eastern and central parts of basins, such as the Transition Domain (between the subarctic and subtropical region) in the NP, which is a major foraging area for pelagic fish. Such diverse activities of various eddies thus also affect ecosystems in each basin. To fully understand the relationships among eddy activity, Chl-*a* distribution, and long-term variation, many challenges remain including the evaluation of sub-meso-scale influences. Further investigation based on higher-resolution data including satellite data, shipboard observations, and numerical models are necessary. Tracking of temporal changes in the internal structures of eddies with profiling floats (e.g., Kaneko et al., 2015) should be continued. Overall, this study contributes to an understanding of the effects of eddies on Chl-*a* patterns in the global ocean.

Acknowledgments

The authors thank the staff of the Mutsu Institute for Oceanography, the Research Institute for Global Change of JAMSTEC, and the Atmosphere and Ocean Research Institute, University of Tokyo. HK and SI were supported by KAKENHI (Grant-in-Aid for Scientific Research on Innovative Areas) Grant Number JP18H03956.

Open Research

Surface current data, the Ocean Surface Current Analysis Real-time third-degree resolution ocean surface currents, are distributed by The Physical Oceanography Distributed Active Archive Center, CA, USA. (https://doi.org/10.5067/OSCAR-03D01). Data for surface CHL-*a* dis-

tributions was provided from GlobColour (http://globcolour.info) developed, validated, and distributed by ACRI-ST, France. Temperature and salinity data were provided by the World Ocean Atlas 2018 (https://accession.nodc.noaa.gov/NCEI-WOA18). Data for outgoing longwave radiation were obtained from NOAA National Climatic Data Center (https://www.ncei.noaa.gov/access/metadata/landing-page/bin/iso?id=gov.noaa.ncdc:C00875).

References

Abraham, E. R. (1998), The generation of plankton patchiness by turbulent stirring, *Nature*, *391*(6667), 577–580. https://doi.org/10.1038/35361

Babin, S. M., J. A. Carton, T. D. Dickey, and J. D. Wiggert (2004), Satellite evidence of hurricane induced phytoplankton blooms in an oceanic desert. *J. Geophys. Res.* 109, 1978–2012. https://doi.org/10.1029/2003JC001938

Bonjean, F., and G. S. E. Lagerloef (2002), Diagnostic model and analysis of the surface currents in the tropical Pacific Ocean. *J. Phys. Oceanogr.*, *32*, 2938–2954. doi: https://doi.org/10.1175/1520-0485(2002)032%3c2938:DMAAOT%3e2.0.CO;2

Boyer, T. P., H. E. Garcia; R. A. Locarnini, M. M Zweng, A. V. Mishonov, J. R. Reagan, K. A. Weathers, O. K. Baranova, C. R. Paver; D. Seidov, I. V. Smolyar (2018), World Ocean Atlas 2018. [indicate subset used]. NOAA National Centers for Environmental Information. Dataset. https://www.ncei.noaa.gov/archive/accession/NCEI-WOA18. Accessed on 19 February 2021.

Browning, T., E. Achterberg, I. Rapp et al. (2017) Nutrient co-limitation at the boundary of an oceanic gyre, *Nature*, *551*, 242–246. https://doi.org/10.1038/nature24063

Byrne, D. A., A. L. Gordon, and W. F. Haxby (1995), Agulhas Eddies: A Synoptic View Using Geosat ERM Data, *J. Phys. Oceanogr.*, *25*, 902–917. https://doi.org/10.1175/1520-0485(1995)025%3c0902:AEASVU%3e2.0.CO;2

Chelton D. B., Schlax M. G., Samelson R. M., and de Szoeke R. A. (2007), Global observations of large oceanic eddies. *Geophys. Res. Lett.*, *34*:L15606. https://doi.org/10.1029/2007GL030812

Chelton, D. B., P. Gaube, M. Schlax, J. Early, and R. Samelson (2011a), The influence of nonlinear mesoscale eddies on near-surface oceanic chlorophyll, *Science*, *334*(6054), 328–332. https://www.science.org/doi/10.1126/science.1208897

Chelton, D. B., M. G. Schlax, and R. M. Samelson (2011b), Global observations of nonlinear mesoscale eddies, *Prog. Oceanogr.*, *91*, 167–216. https://doi.org/10.1016/j.pocean.2011.01.002

Crawford, W. R. (2002), Physical characteristics of Haida eddies. *J. Oceanogr.*, *58*, 703–713. https://doi.org/10.1023/A:1022898424333

Crawford, W. R. (2005), Heat and fresh water transport by eddies into the Gulf of Alaska, *Deep Sea Res. Part II*, *52*, 893–908. https://doi.org/10.1016/j.dsr2.2005.02.003

d'Andon, F. O., A. Mangin, S. Lavender, D. Antoine, S. Maritorena, A. Morel, G. Barrot et al. (2009). "GlobColour - the European Service for Ocean Colour", in Proceedings of the 2009 IEEE International Geoscience & Remote Sensing Symposium, Jul 12–17 2009, Cape Town South Africa: IEEE Geoscience and Remote Sensing Society.

Ducet, N., P. Y. Le Traon, and G. Reverdin (2000), Global high resolution mapping of ocean circulation from Topex/Poseidon and ERS-1 and -2, *J. Geophys. Res.*, *105*, 19477–19498. https://doi.org/10.1029/2000JC900063

Eden, C. (2007), Eddy length scales in the North Atlantic Ocean, *J. Geophys. Res.*, *112*, C06004, https://doi.org/10.1029/2006JC003901

Emery, W.J., and R. E. Thomson (Eds.). (2001), Data Analysis Methods in Physical Oceanography, 1st Edition, 654 pp., Elsevier Science, New York.

Falkowski, P., D. Ziemann, Z. Kolber, and P. Bienfang (1991), Role of eddy pumping in enhancing primary production in the ocean, *Nature*, *352* (6330), 55–58. https://doi.org/10.1038/352055a0

Garcia, C. A. E., Y. V. B. Sarma, M. M. Mata, V. M. T. Garcia (2004), Chlorophyll variability and eddies in the Brazil–Malvinas Confluence region, *Deep Sea Res. Part II*, *51*, 159–172. https://doi.org/10.1016/j.dsr2.2003.07.016

Gaube, P., D. Chelton, P. Strutton, and M. Behrenfeld (2013), Satellite observations of chlorophyll, phytoplankton biomass and Ekman pumping in nonlinear mesoscale eddies, *J. Geophys. Res. Oceans*, *118*, 6349–6370, https://doi.org/10.1002/2013JC009027

Gaube, P., D. J. McGillicuddy Jr., D. B. Chelton, M. J. Behrenfeld, and P. G. Strutton (2014), Regional variations in the influence of mesoscale eddies on near-surface Chlorophyll, *J. Geophys. Res. Oceans*, *119*, 8195–8220, https://doi.org/10.1002/2014JC010111

Gaube, P., and D. J. McGillicuddy Jr. (2017), The influence of Gulf Stream eddies and meanders on near-surface chlorophyll, *Deep Sea Res. Part I*, *122*, 1–16. https://doi.org/10.1016/j.dsr.2017.02.006.

Gill, A. E. (1982), Atmosphere-Ocean Dynamics, 662 pp., Academic Press, San Diego.

Gründlingh, M. L. (1995), Tracking eddies in the southeast Atlantic and southwest Indian oceans with TOPEX/POSEIDON, *J. Geophys. Res.*, *100*, 24977–24986, https://doi.org/10.1029/95JC01985

Hai-Tien Lee, and NOAA CDR Program (2011), NOAA Climate Data Record (CDR) of Daily Outgoing Longwave Radiation (OLR), Version 1.2 (2001–2018). NOAA National Climatic Data Center. doi:10.7289/V5SJ1HH2 [2021/06/09].

Ito, SI., K. Uehara, T. Miyao, H. Miyake, I. Yasuda, T. Watanabe, and Y. Shimizu (2004), Characteristics of SSH Anomaly Based on TOPEX/POSEIDON Altimetry and in situ Measured Velocity and Transport of Oyashio on OICE. *J. Oceanogr.*, *60*, 425–437 https://doi.org/10.1023/B:JOCE.0000038059.54334.6b

Itoh, S, and I. Yasuda (2010), Characteristics of Mesoscale Eddies in the Kuroshio–Oyashio Extension Region Detected from the Distribution of the Sea Surface Height Anomaly, *J. Phys. Oceanogr.*, *40*, 1018–1034. https://doi.org/10.1175/2009JPO4265.1

Johnson, W. K., L. A. Miller, N. E. Sutherland, and C. S. Wong (2005), Iron transport by mesoscale Haida eddies in the Gulf of Alaska, *Deep Sea Res. Part II*, *52*, 933–953, https://doi.org/10.1016/j.dsr2.2004.08.017.

Joyce, T. M. (1984), Velocity and hydrographic structure of a Gulf Stream Warm-Core Ring, *J. Phys. Oceanogr.*, *14*, 936–947, https://doi.org/10.1175/1520-0485(1984)014%3c0936:VAHSOA%3e2.0.CO;2

Kaneko, H., S. Itoh, S. Kouketsu, T. Okunishi, S. Hosoda, and T. Suga (2015), Evolution and modulation of a poleward-propagating anticyclonic eddy along the Japan and Kuril- Kamchatka trenches, *J. Geophys. Res. Oceans*, *120*, 4418–4440, https://doi.org/10.1002/2014JC010693

Kaneko, H., K. Sasaki, H. Abe, T. Tanaka, M. Wakita, S. Watanabe, T. Okunishi, Y. Sato, and S. Tatamisashi (2021), The role of an intense jet in the Tsugaru Strait in the formation of the outflow gyre revealed using high-frequency radar data, *Geophys. Res. Lett.*, https://doi.org/10.1029/2021GL092909

Killworth, P. D., P. Cipollini, B. M. Uz, and J. R. Blundell (2004), Physical and biological mechanisms for planetary waves observed in satellite-derived chlorophyll, *J. Geophys. Res.*, *109*, C07002, https://doi.org/10.1029/2003JC001768

Kouketsu, S., H. Kaneko, T. Okunishi, K. Sasaoka, S. Itoh, R. Inoue, H. Ueno (2016), Mesoscale eddy effects on temporal variability of surface chlorophyll a in the Kuroshio Extension, *J. Oceanogr.*, *72*, 439–451. https://doi.org/10.1007/s10872-015-0286-4

Lehahn, Y., F. d'Ovidio, M. Lévy, Y. Amitai, and E. Heifetz (2011), Long range transport of a quasi isolated chlorophyll patch by an Agulhas ring, *Geophys. Res. Lett.*, *38*, L16610, https://doi.org/10.1029/2011GL048588

Lévy, M., L. Mémery, and G. Madec (1998), The onset of a bloom after deep

winter convection in the northwestern Mediterranean sea: Mesoscale process study with a primitive equation model, *J. Mar. Syst.*, *16*(1), 7–21. https://doi.org/10.1016/S0924-7963(97)00097-3

Lévy, M., P. Klein, and A. M. Treguier (2001), Impact of sub-mesoscale physics on production and subduction of phytoplankton in an oligotrophic regime, *J. Mar. Res.*, *59*, 535–65. https://archimer.ifremer.fr/doc/00000/800/

Lévy, M., R. Ferrari, P. Franks, A. Martin, and P. Rivière (2012), Bringing physics to life at the submesoscale, *Geophys. Res. Lett.*, *39*, L14602. https://doi.org/10.1029/2012GL052756

Lin, I. I., W. T. Liu, C. C. Wu, G. T. Wong, C. Hu, Z. Chen, and K. K. Liu (2003), New evidence for enhanced ocean primary production triggered by tropical cyclone. *Geophys. Res. Lett.*, 30, 1718. https://doi.org/10.1029/2003GL017141

Martin, J. H., R. M. Gordon, S. Fitzwater, and W. W. Brokenow (1989), Vertex: Phytoplankton/iron studies in the Gulf of Alaska. *Deep Sea Res.*, *30*, 649–680.

https://doi.org/10.1016/0198-0149(89)90144-1

Maritorena S., D. A. Siegel, and A. Peterson (2002), Optimization of a Semi-Analytical OceanColour Model for Global Scale Applications. *Appl. Opt.*, *41*, 2705–2714. https://doi.org/10.1364/AO.41.002705

Maritorena, S., and D. A. Siegel (2005), Consistent Merging of Satellite Ocean Colour Data Sets Using a BioOptical Model. *Remote Sens. Environ.*, *94*, 429–440. https://doi.org/10.1016/j.rse.2004.08.014

Maritorena, S., O. Hembise Fanton d'Andon, A. Mangin, and D. A. Siegel (2010), Merged satellite ocean color data products using a bio-optical model: Characteristics, benefits and issues, *Remote Sens. Environ.*, *114*, 1791–1804. https://doi.org/10.1016/j.rse.2010.04.002

McGillicuddy D. J. Jr. (2016), Mechanisms of Physical- Biological-Biogeochemical Interaction at the Oceanic Mesoscale, *Annu. Rev. Mar. Sci.*, *8*, 125–159. https://doi.org/10.1146/annurev-marine-010814-015606

McGillicuddy, D. J. Jr., A. Robinson, D. Siegel, H. Jannasch, R. Johnson, T. Dickey, J. McNeil, A. Michaels, and A. Knap (1998), Influence of meso-scale eddies on new production in the Sargasso Sea, *Nature*, *394* (6690), 263–266. https://doi.org/10.1038/28367

Nilsson, C. S., and G. R. Cresswell (1980), The formation and evolution of East Australian current warm-core eddies, *Prog. Oceanogr.*, *9*, 133–183, https://doi.org/10.1016/0079-6611(80)90008-7

Olson, D. B. (1991), Rings in the Ocean, *Annu. Rev. Earth Planet Sci.*, *19*:1, 283–311. https://doi.org/10.1146/annurev.ea.19.050191.001435

Qiu, B. (1995), Variability and Energetics of the Kuroshio Extension and Its Recirculation Gyre from the First Two-Year TOPEX Data, *J. Phys. Oceanogr.*, *25*, 1827–1842. https://doi.org/10.1175/1520-0485(1995)025%3c1827:VAEOTK%3e2.0.CO;2

Qiu, B. (1999) Seasonal Eddy Field Modulation of the North Pacific Subtropical Countercurrent: TOPEX/Poseidon Observations and Theory, *J. Phys. Oceanogr.*, *29*, 2471–2486. https://doi.org/10.1175/1520-0485(1999)029%3c2471:SEFMOT%3e2.0.CO;2

Qiu, B, and S. Chen (2005), Variability of the Kuroshio Extension Jet, Recirculation Gyre, and Mesoscale Eddies on Decadal Time Scales, *J. Phys. Oceanogr.*, *35*, 2090–2103. https://doi.org/10.1175/JPO2807.1

Ridgway, K. R., and J. R. Dunn (2003), Mesoscale structure of the mean East Australian Current System and its relationship with topography, *Prog. Oceanogr.*, *56*, 189–222. https://doi.org/10.1016/S0079-6611(03)00004-1

Rhines, P. (1975), Waves and turbulence on a beta-plane, *J. Fluid Mech.*, *69*, 417–443. https://doi.org/10.1017/S0022112075001504

Rhines, P. (1977), The Sea, volume 6, chapter The dynamics of unsteady currents, pp. 189–318, John Wiley, Hoboken, N. J.

Siegel, D. (2001), The Rossby rototiller. *Nature*, *409*, 576–577. https://doi.org/10.1038/35054659

Siegel, D., D. Court, D. Menzies, P. Peterson, S. Maritoena, and N. Nelson (2007), Satellite and in situ observation of the bio-optical signatures of two mesoscale eddies in the Sargasso Sea, *Deep Sea Res., Part II*, *55*, 1218–1230. https://doi.org/10.1016/j.dsr2.2008.01.012

Siegel, D., P. Peterson, D. McGillicuddy Jr., S. Maritorena, and N. Nelson (2011), Bio-optical footprints created by mesoscale eddies in the Sargasso Sea, *Geophys. Res. Lett.*, *38*, L13608, https://doi.org/10.1029/2011GL047660

Ueno, H., H. J. Freeland, W. R. Crawford, H. Onishi, E. Oka, K. Sato, and T. Suga (2009), Anticyclonic Eddies in the Alaskan Stream, *J. Phys. Oceanogr.*, *39*, 934–951. https://doi.org/10.1175/2008JPO3948.1

Ueno, H., W. R. Crawford, and H. Onishi (2010), Impact of Alaskan Stream Eddies on chlorophyll distribution in the North Pacific, *J. Oceanogr.*, *66*, 319–328. https://doi.org/10.1007/s10872-010-0028-6

Uz, B., J. Yoder, and V. Osychny (2001), Pumping of nutrients to ocean surface waters by the action of propagating planetary waves. *Nature*, *409*, 597–600. https://doi.org/10.1038/35054527

Whitney, F. A., W. R. Crawford, and P.J. Harrison (2005), Physical processes that enhance nutrient transport and primary productivity in the coastal and open ocean of the subarctic NE Pacific, *Deep Sea Res. Part II*, *52*, 681–706. https://doi.org/10.1016/j.dsr2.2004.12.023.